

# Tracing the Warm-Hot Intergalactic Medium at Low Redshift: X-ray Forest Observations Towards H1821+643

Smita Mathur<sup>1</sup>, David H. Weinberg<sup>1</sup> & Xuelei Chen<sup>2,3</sup>

## ABSTRACT

We present a high resolution ( $\lambda/\Delta\lambda \approx 500$ ) X-ray spectrum of the bright quasar H1821+643 ( $z = 0.297$ ), obtained in a 470 ksec observation with the *Chandra* X-ray Observatory. We search for X-ray absorption by highly ionized metal species, O VII and O VIII in particular, at the redshifts of the six intervening O VI absorption systems known from UV studies. We detect features with  $\gtrsim 2\sigma$  significance at the predicted O VII and O VIII wavelengths of one O VI system, at the O VII wavelength of a second, and at the Ne IX wavelength of a third. We find two additional features of comparable strength (one O VII and one O VIII) within  $1000 \text{ km s}^{-1}$  of O VI redshifts. The  $1\sigma$  constraints on the relative abundances of different species imply significant variations from system to system in  $f(\text{O VI})$ , the fraction of oxygen in the O VI state. The constraints in the two detected O VI systems imply gas overdensities lower than the values  $\delta \gtrsim 100$  expected in virialized systems, suggesting that the absorption arises in lower density, filamentary structures. At the  $2\sigma$  level, however, the physical constraints are weak, though all of the systems must have temperature  $T < 10^6 \text{ K}$  to be consistent with upper limits on O VII. If we treat our  $2\sigma$  detections of known O VI systems as real, but assume minimal O VII and O VIII in the other systems, we estimate  $[f(\text{O VI}) + f(\text{O VII}) + f(\text{O VIII})]/f(\text{O VI}) = 32 \pm 9$  for the average ratio of all highly ionized oxygen species to O VI. Combined with estimates of the total column density of O VI absorption per unit redshift, this ratio implies that the total baryon fraction associated with detected O VI absorbers is  $\Omega_b(\text{O VI}) \sim 0.03h_{70}^{-1}$ , a substantial fraction of the baryon density predicted by big bang nucleosynthesis, and larger than that associated with stars or with gas detected in 21cm or

---

<sup>1</sup>Astronomy Department, The Ohio State University, 140 West 18th Avenue, Columbus, OH 43210; smita, dhw@astronomy.ohio-state.edu

<sup>2</sup>Physics Department, The Ohio State University, 174 West 18th Avenue, Columbus, OH 43210

<sup>3</sup>Institute for Theoretical Physics, U.C. Santa Barbara, Santa Barbara, CA 93106; xuelei@itp.ucsb.edu

X-ray emission. Because of the limited S/N of the detections, these results must be treated with caution. Nonetheless, the combination of the O VI data with these X-ray forest measurements provides the most direct evidence to date for the pervasive, moderate density, shock-heated intergalactic medium predicted by leading cosmological scenarios. The high inferred incidence of relatively strong O VII and O VIII absorption implies that some regions of this medium are enriched to a level substantially above  $[\text{O}/\text{H}] = -1$ .

*Subject headings:* cosmology: observations—galaxies: active—intergalactic medium—quasars: individual (H1821+643)—X-rays: galaxies

## 1. Introduction

Much of our knowledge of the intergalactic medium (IGM) comes from the rest-frame UV line absorption that it imprints on the spectra of background quasars: the Ly $\alpha$  forest of neutral hydrogen and associated metal lines such as C IV and O VI. The Ly $\alpha$  forest is produced mainly by diffuse, photoionized gas at temperatures  $T \sim 10^4$  K, and it appears to trace the main reservoir of cosmic baryons at high redshift (Rauch & Haehnelt 1995; Hernquist et al. 1996; Rauch et al. 1997; Weinberg et al. 1997). The Ly $\alpha$  forest thins out at low redshift, and cosmological simulations predict that the continuing process of structure formation heats a substantial fraction of intergalactic gas to temperatures where it produces little hydrogen Ly $\alpha$  absorption, and where the dominant ionization stages of heavier elements have absorption transitions at X-ray wavelengths rather than UV. Hot, dense gas in the central regions of galaxy clusters and groups can be detected by its X-ray emission, but most of the shock-heated gas resides in the outskirts of virialized halos and in lower density, filamentary structures, making its continuum emission weak. One of the few prospects for detecting this low density, shock-heated gas is via the “X-ray forest” of absorption lines it should produce in quasar spectra (Hellsten, Gnedin, & Miralda-Escudé 1998; Perna & Loeb 1998; Fang & Canizares 2000; Chen et al. 2002; Fang, Bryan, & Canizares 2002a). Nicastro et al. (2002) find strong evidence for absorption by highly ionized oxygen and neon at  $z \approx 0$ , but there have been no clear detections to date of intergalactic X-ray absorption originating beyond the Local Group. This paper describes a search for X-ray forest absorption towards H1821+643 ( $z = 0.297$ ) using a high resolution ( $\lambda/\Delta\lambda \approx 500$ ) spectrum obtained in a 470 ksec observation with the *Chandra* X-ray Observatory.

The baryon density implied by big bang nucleosynthesis and the estimated primordial deuterium abundance,  $\Omega_{\text{BBN}} \approx 0.04h_{70}^{-2}$  (Burles & Tytler 1997, 1998; here  $h_{70} \equiv H_0/70 \text{ km s}^{-1} \text{ Mpc}^{-1}$ ), exceeds the density of baryons in known stars and X-ray emitting gas

by roughly an order of magnitude (Fukugita, Hogan, & Peebles 1998). The lower density regime of the “warm-hot intergalactic medium” (WHIM, a term coined by Cen & Ostriker [1999a] to refer to gas in the temperature range  $10^5 - 10^7$  K) could constitute a major fraction of the “missing” low redshift baryons. Hydrodynamic cosmological simulations predict that 30-50% of the baryons reside in this phase at  $z = 0$  (Cen & Ostriker 1999a; Davé et al. 1999, 2001). HST and FUSE detections of O VI ( $\lambda\lambda 1032, 1038\text{\AA}$ ) absorption lines towards H1821+643 and PG0953+415 (Tripp, Savage, & Jenkins 2000, hereafter TSJ; Tripp & Savage 2000; Oegerle et al. 2000; Savage et al. 2002) offer a tantalizing hint of this baryon reservoir. Adopting conservative assumptions of  $[\text{O}/\text{H}] = -1$  and an O VI ionization fraction  $f(\text{O VI}) = 0.2$  (which is close to the maximum in photo- or collisional ionization), TSJ conclude that the gas associated with these weak O VI absorbers accounts for  $\Omega_b \approx 0.004h_{70}^{-1}$  of the cosmic baryon budget, comparable in total mass to all other known low redshift components combined. They remark, moreover, that  $f(\text{O VI})$  could plausibly be much lower than 0.2, implying a substantially higher baryon fraction. For most reasonable assumptions about the physical conditions of this absorbing gas, the dominant ionization state should be O VII or O VIII. Gas hotter than  $T \sim 5 \times 10^5$  K would have very low  $f(\text{O VI})$ , so it might produce O VII or O VIII absorption with no detectable O VI.

We chose H1821+643 for our X-ray forest search in part because it is one of the brightest X-ray quasar at moderate redshift, and in part because it has been studied carefully for intervening O VI absorption (TSJ; Oegerle et al. 2000). Theoretical expectations for X-ray forest absorption depend strongly on the assumed metallicity distribution of the moderate density, shock-heated IGM, a subject on which there is little empirical guidance. However, for metallicities  $Z \sim 0.1 - 0.3Z_\odot$ , simulations and analytic calculations predict few O VII or O VIII lines above column density  $N \sim 2 \times 10^{15} \text{cm}^{-2}$  (Hellsten, Gnedin, & Miralda-Escudé 1998; Perna & Loeb 1998; Fang & Canizares 2000; Chen et al. 2002; Fang, Bryan, & Canizares 2002a), and weaker absorption by other elements, so even long exposures with *Chandra* or *XMM-Newton* are unlikely to detect absorption at high signal-to-noise ratio. Searching at redshifts with known O VI absorption allows one to adopt a lower effective threshold for significant detection, greatly increasing the odds of success. Furthermore, detections of or upper limits on X-ray absorption provide new constraints on the physical conditions of the O VI absorbers.

We chose the duration of our spectroscopic observation so that if  $[f(\text{O VI}) + f(\text{O VII}) + f(\text{O VIII})]/f(\text{O VI}) \sim 30$ , a physically plausible ratio that would imply that O VI absorbers contain a large fraction of the “missing” low redshift baryons, then we would clearly detect the strongest of the TSJ systems, and we would detect the next two strongest systems at the  $2 - 3\sigma$  level. As we will show below, we find only a  $\sim 1\sigma$  signal from the strongest TSJ system, but we obtain  $\approx 2\sigma$  detections of O VII from the next strongest system and

of O VII and O VIII from the O VI system discovered by Oegerle et al. (2000). We also find features that could correspond to oxygen absorption at other redshifts close to the detected systems (within  $1000 \text{ km s}^{-1}$ ), and a possible signature of Ne IX absorption from one system. The best estimate of the mean  $[f(\text{O VI}) + f(\text{O VII}) + f(\text{O VIII})]/f(\text{O VI})$  from our data is  $\sim 30$ , but the moderate statistical significance of our detections and the implied variation in  $f(\text{O VI})$  from system to system leave the interpretation of our results more ambiguous than we would like. Nonetheless, this observation provides the strongest evidence to date for the moderate density, shock-heated IGM predicted by theoretical models, and the detections and upper limits have important implications for the physical state of the O VI absorption systems and for their connection to the missing baryons of the low redshift universe. We proceed to a description of the observations, data reduction, and absorption line analysis, then to a discussion of these implications.

## 2. Observations and Data Reduction

We observed H1821+643 with *Chandra* between 2001 January 17 and January 24, for a total exposure time of 470 ksec. The observation was divided into four different parts: ObsIDs 2186, 2418, 2310 and 2311. We used the low energy transmission grating (LETG, Brinkman et al. 1997) with the advanced CCD imaging camera for spectroscopy (ACIS-S, C. R. Canizares *et al.* in preparation). Our primary interest is in O VII and O VIII lines with rest wavelengths of  $21.602 \text{ \AA}$  and  $18.969 \text{ \AA}$ , respectively, and thus in the observed wavelength range  $18.9\text{--}28 \text{ \AA}$  that runs from O VIII at  $z = 0$  to O VII at the quasar redshift  $z = 0.297$ . Since the lines are expected to be low S/N, it is important to optimize the instrument response in this interval. To avoid the S3/S4 chip gap between  $21.2$  and  $21.8 \text{ \AA}$ , the aim point was offset by  $2'$  in +Y direction. This offset moves the chip gap to  $27.9\text{--}28.5 \text{ \AA}$ , so the entire first order spectrum in the wavelengths of interest is now on S3. Since the telescope focus is on S3, this choice enhances the effective area around  $25 \text{ \AA}$ . To ameliorate the effects of CTI for spectral order sorting, a SIM-Z offset of  $-8 \text{ mm}$  was chosen. Accordingly, an ACIS-S subarray with rows 49–256 was used.

The shift of aimpoint, essential for optimizing wavelength coverage and effective area in the most interesting part of the spectrum, had the additional effect of placing the zeroth-order grating image close to the S2/S3 chip gap. This is not a concern from the scientific point of view, since the X-ray forest search relies on the high resolution, dispersed spectrum. However, the standard *Chandra* processing software (*Chandra* Interactive Analysis of Observations, CIAO, Elvis et al. in preparation) failed to process the data properly as a result of this non-standard aim-point. In particular, the CIAO tool `tg_resolve_events`, which assigns a

wavelength and an order to each observed photon, failed. This problem was fixed in CIAO version 2.2, and the data were reprocessed to recover all of the observed photons. We used CIAO version 2.2 in all the data reduction and analysis.

We extracted spectra from each of the four observations separately,<sup>4</sup> and +1 and –1 orders were co-added. The four resulting spectra were then co-added to construct the full first-order spectrum. Errors in observed counts were appropriately propagated. The net observed count rate is 0.428 counts per second for the combined first-order spectrum, with  $2 \times 10^5$  total net counts. The unbinned spectrum has 8192 wavelength channels with  $\Delta\lambda = 0.0125$  Å. The full width at half maximum of the line response function is about 0.05Å, increasing to larger values longward of about 50Å. The spectral resolution is therefore  $\lambda/\Delta\lambda \approx 500$  at 25Å. The data span the wavelength range from 1 to 60 Å, but there is essentially no detectable flux longward of  $\sim 40$ Å. The understanding of the absolute wavelength calibration of *Chandra* spectra is continually evolving,<sup>5</sup> but the best current evidence is that the measured wavelengths near 25Å are offset with respect to true wavelengths by an amount  $0 \leq \Delta\lambda \leq 0.025$ Å. While we could add a 0.0125Å offset to all measured wavelengths and thereby make the calibration uncertainty symmetric about zero, we have chosen instead to keep the standard wavelength scale and to consider an observed feature “matched” to a predicted feature at wavelength  $\lambda_p$  if it lies between  $\lambda_p$  and  $\lambda_p + 0.025$ Å.

### 3. Analysis

In order to detect and measure absorption lines, we first need an accurate model of the unabsorbed continuum. The continuum properties of H1821+643 have been discussed by Fang et al. (2002b), so we will not examine them in detail here. We obtain a continuum for purposes of line detection by fitting a smooth model to the coarsely binned first-order spectrum. The model that we fit is

$$f(E) = K \left( \frac{E}{1 \text{ keV}} \right)^{-\Gamma} \exp[-N_H \sigma(E)], \quad (1)$$

representing power-law emission absorbed by Galactic gas with hydrogen column density  $N_H$  and bound-free absorption cross-section  $\sigma(E)$ . However, we found that a single power law did not provide an adequate fit over the entire range of the data, and we therefore

---

<sup>4</sup>See [http://cxc.harvard.edu/ciao/documents\\_threads\\_gspec.html](http://cxc.harvard.edu/ciao/documents_threads_gspec.html)

<sup>5</sup>See <http://cxc.harvard.edu/cal/calreview/>

carried out two independent fits in the range 0.3–0.7 keV (17.7–41.3Å) and 0.6–1 keV (12.4–20.7Å). We use the first fit to search for lines in the O VII and O VIII region, and the second to search for lines in the Ne IX and Ne X region. Obtaining an adequate representation of the data further requires that we treat the column density  $N_H$  as a free parameter rather than adopting the standard value of  $3.9 \times 10^{20} \text{ cm}^{-2}$  (Lockman & Savage 1995); in effect, we use  $N_H$  as a parameter to describe departures from a power law, whether intrinsic to the quasar or caused by the Galactic ISM. The fit parameters are: in the 0.3–0.7 keV region,  $K = 0.0030 \text{ photons keV}^{-1} \text{ cm}^{-2} \text{ s}^{-1}$ ,  $\Gamma = 2.28$ ,  $N_H = 5.67 \times 10^{20} \text{ cm}^{-2}$ ; in the 0.6–1 keV region,  $K = 0.0035 \text{ photons keV}^{-1} \text{ cm}^{-2} \text{ s}^{-1}$ ,  $\Gamma = 2.08$ ,  $N_H = 3.69 \times 10^{20} \text{ cm}^{-2}$ . Both of these fits have  $\chi^2/\text{d.o.f.} \sim 1$ , but visual inspection reveals some excess flux between 24 and 25Å (see Figure 2, top), which we have chosen to model as two Gaussian “emission lines” centered at 24.1516Å and 24.5629Å, with FWHM of 0.3035Å and 0.120844Å, respectively. The amplitudes of these features (i.e., the integrals under the Gaussians) are  $1.795 \times 10^{-5}$  and  $9.601 \times 10^{-6} \text{ photons cm}^{-2} \text{ s}^{-1}$ , respectively. The nature of these “emission lines” is unclear. We analyzed several data sets from the *Chandra* archive that had similar LETG/ACIS-S instrument set-ups to look for possible systematic calibration problems, but these do not show signs of excess flux at these wavelengths. We expect, therefore, that this flux originates either from the quasar itself or from the surrounding cluster. A physical characterization is not essential to our purposes here, since we only need to define a smooth continuum that fits our data.

Our final continuum model, therefore, consists of one of the two absorbed power laws described above (depending on the wavelength region), with the additional Gaussian emission lines in the 24–25Å region, all modulated by the instrument response, which we fold in by creating an “arf” file generated for our observational set-up. We began our search for potential X-ray forest systems by examining the residuals between the data and this smooth continuum model, looking for correlations between minima of the residual spectrum and the absorption wavelengths expected on the basis of the known O VI systems. Figure 1 shows the residual spectrum in the 21–28Å region, where the associated O VII and O VIII lines fall. The spectrum in the upper panel has been convolved with a beta function of FWHM=0.05Å, which represents the line response function (LRF) of the instrument at these wavelengths. This smoothing suppresses uncorrelated noise fluctuations relative to features that have the expected shape of true, unresolved absorption (or emission) lines, and it should therefore enhance the contrast of physical absorption features relative to photon noise. However, LRF convolution systematically broadens features and reduces their central depth (while preserving their equivalent width), so in the lower panel we show the residual spectrum smoothed instead with a Savitsky-Golay (S-G) filter (see Press et al. 1992, section 14.8). This type of filter approximately preserves the sharpness and depth of features, but it is less

effective at suppressing noise. The two approaches have complementary advantages, and in practice the two residual spectra show significant features at nearly the same locations.

The strong line at  $\lambda \approx 23.5\text{\AA}$  is Galactic O I, and at somewhat shorter wavelengths, the Galactic O-K edge and features of the instrument response cause rapid variation of the model continuum (see Figure 2, top panel). The blue box running from 22.2–23.6 $\text{\AA}$  marks the wavelength region where these complications make reliable determination of residuals difficult. We have normalized the residuals of the two smoothed spectra so that, in each case, the range  $-1$  to  $+1$  contains 68% of the data points between 21 $\text{\AA}$  and 27.7 $\text{\AA}$ , excluding this problematic region. Dotted horizontal lines mark the symmetric range about zero that contains 90% (upper panel) or 95% (lower panel) of the data points in the same wavelength regions. Solid vertical line segments mark the expected positions of the  $\lambda 21.602\text{\AA}$  line of O VII (green) and the  $\lambda 18.969\text{\AA}$  line of O VIII (red) at the redshifts of the O VI systems found by TSJ and Oegerle et al. (2000):  $z = 0.26659, 0.24531, 0.22637, 0.22497, 0.21326,$  and  $0.12137$ . For brevity, we will often refer to these redshifts simply as z1–z6, in descending order (right to left in Figure 1). Squares below the line segments in the upper panel have an area proportional to the equivalent width of the  $\lambda 1032\text{\AA}$  O VI line reported by TSJ or Oegerle et al. (2000). The wavelength calibration uncertainty  $\Delta\lambda = 0.025\text{\AA}$  corresponds to two channels in these histogram plots. As discussed in §2, this uncertainty is not symmetric, and we expect a line associated with a given O VI system to appear in the predicted channel or in one of the two channels to its right (at higher  $\lambda$ ). In velocity units, one channel is  $0.0125\text{\AA} \times (c/\lambda)/(1+z) \sim 125 \text{ km s}^{-1}$  (at  $z = 0.2, \lambda = 25\text{\AA}$ ), and the wavelength calibration uncertainty is  $\sim 250 \text{ km s}^{-1}$ .

Visual inspection of either panel of Figure 1 shows that three of the deepest minima occur within the 2-channel wavelength calibration uncertainty of the z2 and z6 O VII wavelengths and the z6 O VIII wavelength (26.901 $\text{\AA}$ , 24.224 $\text{\AA}$ , and 21.271 $\text{\AA}$ , respectively). Subsequent analysis (described below) shows the presence of absorption features that are significant at the  $\gtrsim 2\sigma$  level at these wavelengths, so we classify these systems as probable detections and mark them with filled symbols in the upper panel of Figure 1. The strongest O VI system lies at z4=0.22497, and it has a weaker neighbor at z3=0.22637. There is a strong minimum in the residual spectrum just redward of the predicted O VII wavelengths, but it is not consistent with lying at either of the O VI redshifts. Since this line is comparable in significance to the O VII lines at z2 and z6, and since it lies within  $1000 \text{ km s}^{-1}$  of the strongest O VI system (and within  $650 \text{ km s}^{-1}$  of the weaker system at z3), we consider it a candidate for an O VII system at a nearby, but previously unknown, absorption redshift, and we mark it by dotted green vertical line segments in Figure 1. In similar fashion, we consider the feature  $\sim 1000 \text{ km s}^{-1}$  redward of the apparent O VIII line at z6 to be a candidate for a new O VIII absorption line, marked by the dotted vertical red segments. There are no strong signals near the redshifts

of the other O VI systems. The O VIII wavelength of the z2 system,  $\lambda = 23.622\text{\AA}$ , lies close to the Galactic O I absorption line, but we still would have been able to detect a separate line if it were present and strong. There is a strong feature at  $\lambda \approx 25.35\text{\AA}$  for which we have no clear identification. Its strength and breadth make it unlikely to be intervening O VII.

For quantitative assessment of features and measurement of line parameters, it is preferable to work with the unsmoothed, directly observed spectrum. Figure 2 shows the 21–28 $\text{\AA}$  region of the observed spectrum, with no extra smoothing or binning. Starting with O VII, we added to our continuum model a Gaussian absorption line at the  $\lambda 21.602\text{\AA}$  wavelength for each of the O VI redshifts z1 to z6. The intrinsic FWHM of each line was fixed to be  $100\text{ km s}^{-1}$ , similar to that of the O VI lines (TSJ); the precise value of the line width is unimportant, since the lines are unresolved if they are narrower than  $\sim 250\text{ km s}^{-1}$ . The normalizations of the absorption lines were thus the only new free parameters, which we determined by fitting the continuum plus absorption lines model to the observed spectrum (using the continuum parameters determined previously from the coarsely binned data), folding in the effective area and the line response function. We performed this and all subsequent fits using the “sherpa” software within CIAO-2.2.

This fit yielded non-zero normalizations of the absorption lines at z2, z4, and z6, but not at z1, z3, or z5, just as one might expect from visual inspection of Figure 1. To allow for the wavelength calibration uncertainty and for the possibility of small velocity offsets between O VI and O VII/O VIII absorption, we refit the spectrum allowing the positions of the z2, z4, and z6 lines to vary. This fit yielded offsets of  $\Delta\lambda = +0.0111\text{\AA}$  and  $+0.0274\text{\AA}$  at z2 and z6, within the wavelength calibration uncertainty, while the offset at z4 was significantly larger. We then repeated the model fit a final time, this time fixing the z2 and z6 line positions to these best-fit values and the z4 line position to the original value based on the O VI redshift, with the normalizations of the z2, z4, and z6 systems as the free parameters. Table 1 lists the corresponding equivalent widths of the three fitted lines. The reduction in  $\chi^2$  obtained by adding each of the three lines is  $\Delta\chi^2 = 4.8, 1.27, \text{ and } 2.68$ , with a corresponding  $F$ -test statistical significance (for one additional degree of freedom in each case) of 99.28%, 83.8%, and 95.8%, respectively. We therefore classify the z2 and z6 lines, but not the z4 line, as probable detections, significant at the  $2 - 3\sigma$  level. The  $1\sigma$  error bars quoted in Table 1 correspond to  $\Delta\chi^2 = 1$  relative to the model with best-fit parameters.

Applying the same procedure at the expected wavelengths of the O VIII  $\lambda 18.969\text{\AA}$  line yielded a significant detection at z6, a non-zero value at z2, and best-fit normalizations of zero at the other O VI redshifts, just as expected from Figure 1. For the z6 line, there is a wavelength offset of  $+0.0242\text{\AA}$ , and the reduction in  $\chi^2$  is 3.51, giving an  $F$ -test significance of 98.03%. The z2 line reduces  $\chi^2$  by 1.08 (significance 80.4%).



We also searched for absorption in the same way at the expected wavelengths of the Ne IX  $\lambda 13.447\text{\AA}$  and Ne X  $\lambda 12.1337\text{\AA}$  lines. This analysis yielded a line at the Ne IX wavelength at redshift  $z_4$ , with  $\Delta\chi^2 = 4.86$ , and an  $F$ -test significance for one additional degree of freedom of 98.3%. The existence of detectable Ne IX for this system, which has at best weak O VII and O VIII absorption, would be remarkable, implying non-solar abundance ratios. Nicastro et al. (2002) find evidence for super-solar Ne/O at  $z \sim 0$ . If the Ne IX detection here is real, the implied Ne/O ratio for this system would be higher still. There were no significant detections of Ne IX or Ne X lines for any of the other O VI systems, nor of X-ray lines from C IV, C V, N VI, or N VII.

We determined  $1\sigma$  upper limits on the strength of the O VII, O VIII, and Ne IX lines at the redshifts of the remaining O VI systems by adding lines at the expected wavelength and finding the amplitude that produced  $\Delta\chi^2 = 1$  relative to the smooth continuum model. These upper limits are listed in Table 1. The O VIII limits for the  $z_3$ ,  $z_4$ , and  $z_5$  systems are somewhat less secure than the others because of the complicated form of the continuum in this wavelength region. We also fit line parameters for the two candidate “new” systems discussed earlier, one close to the  $z_3$ - $z_4$  O VII wavelength (with  $z = 0.229048$ ) and one close to the  $z_6$  O VIII wavelength (with  $z = 0.125847$ ). The derived equivalent widths and  $1\sigma$  error bars for these systems are listed in Table 2. Although these systems lie within  $\sim 1000 \text{ km s}^{-1}$  of known O VI redshifts, this condition is much less stringent than that of matching within the  $0 - 250 \text{ km s}^{-1}$  wavelength calibration uncertainty, making the probability of chance coincidence much higher. We therefore attribute substantially less significance to these two candidate systems, even though they are comparable in strength to the “detected” O VII and O VIII lines listed in Table 1.

Our final model for the 21–28 $\text{\AA}$  region of the spectrum, therefore, consists of the continuum model described previously, plus O VII absorption lines at  $z_2$ ,  $z_4$ ,  $z_6$ , and the “new” absorption redshift  $z = 0.229048$ , plus O VIII absorption lines at  $z_2$ ,  $z_6$ , and the “new” redshift  $z = 0.125847$ . The  $z_4$  O VII and  $z_2$  O VIII features are different from zero at the  $\sim 1\sigma$  level, while the other features are different from zero at the  $\gtrsim 2\sigma$  level. Figure 2 shows the observed spectrum and this continuum+lines model, over the full 21–28 $\text{\AA}$  region, and in close-up views near the absorption redshifts. Figure 3 shows the 14–18 $\text{\AA}$  region in the same fashion. Here the model consists of the continuum with a single Ne IX absorption line at  $z_4$ , which is different from zero at the  $2 - 2.5\sigma$  level.

Since the signals we are looking for are weak, and the detection of even one X-ray forest system of great physical import, we have been as meticulous as possible in our data reduction and analysis. In addition to the analysis reported here, we analyzed several data sets in the *Chandra* archive that have similar instrument set-up to search for any hidden

systematic effects, e.g., instrumental features that would produce artificially low counts in the neighborhood of our detected lines. We found no evidence for any such effects, and we are therefore confident that the features seen in Figures 1–3 are true properties of the data, not artifacts of the observational or analysis procedures.

The existence of features with  $\gtrsim 2\sigma$  significance at several wavelengths predicted *a priori* on the basis of O VI absorption suggests that we have indeed detected X-ray forest lines from highly ionized oxygen in these systems. However, we cannot rule out the possibility that the coincidence between observed features and known absorption redshifts is, in fact, just a coincidence. It is difficult to estimate the probability of obtaining our results “by chance” if there were no true signals in the spectrum, since the novelty of the observation was such that we could not define clear “detection” criteria in advance of seeing the data. Very roughly, we can note that 3 of the 12 strongest negative deviations in the 21–28Å region of the residual spectrum lie within the 0.025Å wavelength calibration uncertainty of a known O VI redshift. (This is true for either of the residual spectra shown in Figure 1.) Excluding the problematic 22.2–23.6Å region, there are about 450 channels in this spectral range, and nine absorption wavelengths (six O VII and three O VIII) that could serve as possible “matches” to a given feature. The wavelength calibration uncertainty gives any of the expected absorption wavelengths a 3-channel range for a “match,” so the probability that a randomly selected channel in this wavelength range matches one expected absorption system is about  $9 \times 3/450 = 0.06$ . The probability of getting 3 of the 12 strongest deviations matched with known redshifts, in the absence of a true physical correlation, is then  $(0.06)^3$  multiplied by  $12!/(9! \times 3!) = 220$  (the number of ways that one can choose 3 distinct objects from a set of 12), or about 5%. Since this probability is not extremely small, we will be cautious in interpreting our observations, considering both the possibility that we have true detections of several X-ray forest absorbers and the possibility that we have only upper limits. The only way to remove this ambiguity is to obtain a higher S/N spectrum with a longer observation.

#### 4. Implications

The high density of weak O VI absorbers establishes them as an important constituent of the low redshift universe. TSJ estimate  $dN/dz \sim 48$  for O VI absorbers with rest-frame equivalent width  $W_r \gtrsim 30 \text{ mÅ}$ , based on *HST*/STIS observations of the H1821+643 sightline. While the statistical error on this estimate is large because of the small number of systems, the discovery of an additional low- $z$  O VI system by Oegerle et al. (2000) and of a comparable line density towards PG0953+415 by Savage et al. (2002) supports the inference of a high

cosmic incidence of O VI absorption (see Savage et al. 2002 for discussion). By constraining the absorption produced by more highly ionized oxygen species, our X-ray data provide valuable new constraints on the physical state of the O VI absorbers.

As emphasized by Hellsten, Gnedin, & Miralda-Escudé (1998), photoionization by the cosmic X-ray background can have an important impact on the fractional abundance of O VII and O VIII at moderate overdensities, and photoionization by the UV background can strongly influence the fractional abundance of O VI. We therefore follow the methodology of Chen et al. (2002) and calculate  $f(\text{O VII})/f(\text{O VI})$  and  $f(\text{O VIII})/f(\text{O VI})$  as a function of density and temperature using the publicly available code CLOUDY (Ferland 1999), incorporating photoionization by the UV background as estimated by Shull et al. (1999) and the soft X-ray background estimated by Miyaji et al. (1998). Figure 4 shows the fractional abundance of O V, O VI, O VII, and O VIII as a function of temperature for collisional ionization and for collisional + photoionization in gas with hydrogen number density  $n_H = 10^{-6}\text{cm}^{-3}$ ,  $10^{-5}\text{cm}^{-3}$ , and  $10^{-4}\text{cm}^{-3}$ . For  $\Omega_b h_{70}^2 = 0.04$ , these physical densities correspond to overdensities  $\delta_b \equiv \rho_b/\bar{\rho}_b = 6/(1+z)^3$ ,  $60/(1+z)^3$ , and  $600/(1+z)^3$ , respectively. For reference, the overdensity at the “virial boundary” of a collapsed halo is  $\delta \sim 50 - 150$  in a flat universe with a cosmological constant and  $\Omega_m \sim 0.3$ , with the precise value depending on the halo profile and on the adopted definition of the virial radius (see, e.g., Navarro et al. 1997). At low temperatures and low densities, the fractional abundances are strongly influenced by photoionization, while at higher temperatures and densities they approach the abundances expected in collisional equilibrium.

Figure 5 translates these results into contours in the  $f(\text{O VIII})/f(\text{O VI})$  vs.  $f(\text{O VII})/f(\text{O VI})$  plane. In the left panel, curves show tracks at physical densities that correspond to  $\delta_b(1+z)^3 = 1, 10, 10^2$ , and  $10^3$ , with an additional track for collisional ionization. Numbers along the tracks mark temperatures  $\log T = 4.5, 5.0, 5.5, 6.0$ ; for  $T \geq 10^{6.5}$  K,  $f(\text{O VII})/f(\text{O VI}) > 1000$  for any overdensity. The right panel shows lines of constant temperature. For  $T \lesssim 10^{5.2}$  K, the ion ratios follow a diagonal track in this plane that is essentially independent of temperature. As  $T$  increases, the tracks become more vertical, separating along the  $f(\text{O VII})/f(\text{O VI})$  dimension. Comparing the two panels shows that  $f(\text{O VII})/f(\text{O VI})$  is primarily a diagnostic of gas temperature, while  $f(\text{O VIII})/f(\text{O VI})$  constrains the gas density for a given value of  $f(\text{O VII})/f(\text{O VI})$ . This behavior reflects the competing roles of photoionization and collisional ionization, with the latter being more important for higher temperatures, higher densities, and lower ionization states.

To estimate  $f(\text{O VII})/f(\text{O VI})$  and  $f(\text{O VIII})/f(\text{O VI})$  for the observed systems, we need to convert line equivalent widths to corresponding column densities for each ion species. The second column of Table 3 lists the O VI column densities and  $1\sigma$  error bars that TSJ and

Oegerle et al. (2000) derive by fitting profiles of the 1032Å line. Our data do not have the resolution and S/N required for profile fitting, so we instead infer O VII and O VIII column densities using the relations for optically thin lines,

$$N(\text{O VII}) = 3.48 \times 10^{15} \text{cm}^{-2} \left( \frac{W_{\text{thin}}}{10 \text{ mÅ}} \right), \quad (2)$$

$$N(\text{O VIII}) = 7.56 \times 10^{15} \text{cm}^{-2} \left( \frac{W_{\text{thin}}}{10 \text{ mÅ}} \right), \quad (3)$$

where  $W_{\text{thin}}$  is the rest-frame equivalent width (note that the observed-frame equivalent widths in Tables 1 and 2 must be divided by  $1+z$  before applying these relations). Equations (2) and (3) are based on oscillator strengths of 0.70 and 0.42 for O VII  $K\alpha$  and O VIII  $K\alpha$ , respectively, taken from Verner, Verner, & Ferland (1996). Columns 3 and 4 of Table 3 list the corresponding column density estimates with  $1\sigma$  error bars, or  $1\sigma$  upper limits for lines with a best-fit equivalent width of zero. The z2 system has an inferred O VII column density of  $3.9 \pm 1.7 \times 10^{15} \text{cm}^{-2}$ , while the z6 system has  $N(\text{O VII}) = 2.8 \pm 1.5 \times 10^{15} \text{cm}^{-2}$  and  $N(\text{O VIII}) = 6.7 \pm 3.5 \times 10^{15} \text{cm}^{-2}$ . These are consistent with the upper limits derived by Fang et al. (2002b) from a short *Chandra* exposure. Upper limits for undetected systems are typically  $\sim 1.9 \times 10^{15} \text{cm}^{-2}$  for O VII and  $\sim 3 \times 10^{15} \text{cm}^{-2}$  for O VIII. The simulations of Chen et al. (2002) suggest that saturation effects for typical lines are small ( $\lesssim 30\%$ ) at column densities  $N(\text{O VII}) \leq 4 \times 10^{15} \text{cm}^{-2}$  or  $N(\text{O VIII}) \leq 10^{16} \text{cm}^{-2}$ . We therefore expect saturation corrections to be unimportant in the case of our upper limits and limited but not entirely negligible in the case of our detections. Figure 6 shows the curve-of-growth relation for O VII and O VIII lines with  $b$  parameters in the range  $50 - 250 \text{ km s}^{-1}$ , from which one can read off the column density as a function of (rest-frame) equivalent width for an assumed value of  $b$ .

In Figure 5, points with  $1\sigma$  error crosses mark the two detected O VI systems at z2 and z6, with ion ratios based on the numbers in Table 3. Since the fractional errors in O VI column densities are far smaller than those in the O VII or O VIII column densities, we have ignored them in calculating the errors on column density ratios. For the remaining four systems, we plot arrows showing the  $1\sigma$  upper limits on  $f(\text{O VII})/f(\text{O VI})$  and  $f(\text{O VIII})/f(\text{O VI})$ . Since the upper limits on the strength of the X-ray forest lines are roughly constant from system to system, the upper limits on the ion ratios are, to a first approximation, inversely proportional to the O VI column density. The main exception is the O VII line of the z4 system, for which the best-fit column density is  $1\sigma$  different from zero. The best-fit  $f(\text{O VII})/f(\text{O VI})$  ratio of this system lies near the left-hand edge of the horizontal arrow.

At the  $\sim 1\sigma$  level, our measurements and limits have a number of interesting implications. First, there are variations in the ion ratios from system to system: the lower limit on

$f(\text{O VII})/f(\text{O VI})$  for the z2 system is above the upper limit for the z4 and z1 systems, and the lower limit on  $f(\text{O VIII})/f(\text{O VI})$  for the z6 system is above the upper limit for the z4 system. Given the sensitivity of the abundance ratios to density and temperature, it is not particularly surprising to find that they vary from system to system, but these results suggest that the diversity in physical properties will be important in understanding the contribution of O VI systems to the baryon budget. The z2 and z6 systems have higher  $N(\text{O VI})/N(\text{H I})$  than the other four systems (TSJ; Oegerle et al. 2000), perhaps implying higher gas temperatures that also account for the higher relative abundance of O VII and O VIII. Second, the upper limits on the undetected systems restrict their locations in the temperature-density plane — roughly speaking, the absence of detectable O VII provides an upper limit on the gas temperature, and the absence of detectable O VIII provides a lower limit on the gas density for a given temperature. For example, the z4 system must have  $T \lesssim 10^{5.5}$  K, and if it is close to this temperature, it must have  $\delta_b \gtrsim 5$ . Third, the overdensities implied by the best-fit line parameters of the detected systems at z2 and z6 are significantly below the values  $\delta_b \sim 100$  corresponding to virialized systems. In physical terms, the co-existence of detectable amounts of O VI, O VII, and O VIII requires that photoionization play a central role in determining the abundance ratios, which is possible only if the density is fairly low.

The last of these conclusions is the most interesting, and also the most surprising. In the case of the z2 absorber, the density implied by the best-fit abundance ratios is  $n_H \sim 10^{-5} \text{cm}^{-3}$ , corresponding to  $\delta_b(1+z)^3 \sim 60$ . If we assume that  $f(\text{O VII}) + f(\text{O VIII}) \approx 1$ , then the path length required to produce the estimated column density  $N(\text{O VII}) + N(\text{O VIII}) = 7.1 \times 10^{15} \text{cm}^{-2}$  is  $L = 3 \text{ Mpc } (Z/0.1Z_\odot)^{-1}$ , where  $Z$  is the metallicity and we take solar relative abundances,  $n_O/n_H = 7.41 \times 10^{-5} (Z/0.1Z_\odot)$ , from Verner, Verner, & Ferland (1996). This path is rather long for a system of  $T \sim 10^{5.8}$  K, unless the metallicity is significantly above  $0.1Z_\odot$ , but the ion ratios of this system are consistent at the  $1\sigma$  level with a density an order-of-magnitude higher, which would reduce the implied path length by the same factor. The z6 system is more of a puzzle. Taking  $\delta_b(1+z)^3 \sim 10$  (higher than the best-fit value, but easily within the  $1\sigma$  error bar), the path length implied by a similar calculation is  $L \sim 24 \text{ Mpc } (Z/0.1Z_\odot)^{-1}$ , which would be long even for  $Z = Z_\odot$ .

One possibility, of course, is that the true abundance ratios of this system lie outside the range of our  $1\sigma$  error estimates. In particular, if  $f(\text{O VIII})/f(\text{O VI})$  is substantially lower than our estimate, then the density of the system could be much higher, and the implied path length shorter. The implied density would also be higher if the inferred O VII column density has been artificially depressed by saturation. A third possibility is that the absorber is multi-phase, with the O VIII (and perhaps O VII) absorption arising in hotter gas. In this case, the ion ratios do not yield accurate constraints on the density. Higher S/N observations could rule out (or confirm) the first possibility, and good constraints on the line width from

UV observations could address the second, but the last is an unavoidable source of systematic uncertainty in the interpretation of measurements like these.

Unfortunately, our constraints at the  $2\sigma$  level are rather weak. The O VII and O VIII fractions of the detected systems are consistent with zero at the  $\sim 2\sigma$  level. One can see the approximate  $2\sigma$  upper limits for these systems in Figure 5 by adding  $\log 3/2 \approx 0.18$  to the points. Similarly, one obtains approximate  $2\sigma$  upper limits for the undetected systems by adding  $\log 2 \approx 0.3$  to the  $1\sigma$  upper limits shown in Figure 5. The conclusion that  $T < 10^6$  K, with a tighter upper limit for stronger absorbers, holds robustly, but stronger physical constraints on the O VI systems at the  $2\sigma$  level require higher S/N than our present observations afford.

What can we say about the contribution of O VI absorbers to the cosmic baryon budget? TSJ estimate this contribution based on their STIS observations of H1821+643, using the equation

$$\Omega_b(\text{O VI}) = \frac{\mu m_H H_0}{\rho_c c} \frac{1}{\Delta X} \left(\frac{\text{O}}{\text{H}}\right)^{-1} \langle [f(\text{O VI})]^{-1} \rangle \sum_i N_i(\text{O VI}) . \quad (4)$$

Here  $\rho_c$  is the critical density,  $\Delta X$  is the absorption distance interval (Bahcall & Peebles 1969) probed by the observations, and  $N_i(\text{O VI})$  is the O VI column density in system  $i$ . The factor  $(\text{O}/\text{H})^{-1}[f(\text{O VI})]^{-1}$  converts the O VI column density of a system to the hydrogen column density, and the average represented by  $\langle \dots \rangle$  should be weighted by O VI column density for equation (4) to hold. In fact,  $(\text{O}/\text{H})^{-1}$  should be inside the  $\langle \dots \rangle$  as well, but since our observations give no additional purchase on the metallicity, we will assume that it is constant from system to system. Adopting uniform values of  $[\text{O}/\text{H}] = -1$  and  $f(\text{O VI}) = 0.2$ , TSJ find  $\Omega_b(\text{O VI}) = 0.0043 h_{70}^{-1}$ . Since  $f(\text{O VI}) = 0.2$  is close to the maximum possible O VI fraction, TSJ interpret this estimate as a lower limit on  $\Omega_b(\text{O VI})$  for  $[\text{O}/\text{H}] = -1$ . More generally, we can express the TSJ result as

$$\Omega_b(\text{O VI})_{\text{TSJ}} = 0.0043 h_{70}^{-1} \left(\frac{0.1}{10^{[\text{O}/\text{H}]}}\right) \left(\frac{\langle [f(\text{O VI})]^{-1} \rangle}{5.0}\right) . \quad (5)$$

Subsequent observations of three other sight lines (Richter et al. 2001; Sembach et al. 2001; Savage et al. 2002) suggest that the density of O VI absorbers towards H1821+643 may be higher than average, and that the TSJ estimate should perhaps be revised downwards by about a factor of two (Savage et al. 2002).

While small number statistics and the unknown metallicity are both significant sources of uncertainty in the  $\Omega_b(\text{O VI})$  estimates, the major uncertainty in equation (4) is the O VI ionization fraction, since  $\langle [f(\text{O VI})]^{-1} \rangle$  could quite plausibly be an order-of-magnitude larger than the factor of 5.0 adopted by TSJ. However, since  $f(\text{O VI}) + f(\text{O VII}) + f(\text{O VIII})$  should

be close to unity in most systems that have detectable O VI (see Figure 4), it is just this factor that the *Chandra* spectrum allows us to estimate:

$$\langle [f(\text{O VI})]^{-1} \rangle \approx \frac{\sum_i N_i(\text{O VI}) + N_i(\text{O VII}) + N_i(\text{O VIII})}{\sum_i N_i(\text{O VI})}. \quad (6)$$

The sums in equation (6) weight  $[f(\text{O VI})]^{-1}$  by O VI column density, as desired for the  $\Omega_b(\text{O VI})$  estimate.

For our *estimate* of  $\langle [f(\text{O VI})]^{-1} \rangle$ , we use the measured values of  $N(\text{O VII})$  and  $N(\text{O VIII})$  for the z6 system and of  $N(\text{O VII})$  for the z2 system; we use  $N(\text{O VIII}) = 0$  for the z2 system, and we set  $N(\text{O VI}) + N(\text{O VII}) + N(\text{O VIII}) = 5N(\text{O VI})$  for the other four systems. In other words, we treat all of our  $2\sigma$  detections as real, but where we have only  $1\sigma$  measurements or upper limits, we conservatively assume the lowest O VII and O VIII column densities consistent with the physical expectation that  $f(\text{O VI}) \leq 0.2$ . To obtain a  $1\sigma$  error bar on this estimate, we sum the errors of the three detected X-ray lines in quadrature, and we ignore the much smaller contribution from uncertainty in the O VI column densities. This calculation yields  $\langle [f(\text{O VI})]^{-1} \rangle = 32 \pm 9$ . Combined with the TSJ result (eq. 5), this ratio implies  $\Omega_b(\text{O VI}) = 0.028 \pm 0.008 h_{70}^{-1}$  for  $[\text{O}/\text{H}] = -1$ .

The statistical error bar here accounts *only* for the observational uncertainties in the  $N(\text{O VII})$  and  $N(\text{O VIII})$  measurements, not the uncertainty due to the small number of systems along the single line of sight employed in the analysis, which is probably at least as important. Furthermore, each of our detected features is consistent with zero at the  $\sim 2\sigma$  level, and we cannot rule out the possibility that the apparent association between these features and O VI redshifts is coincidental. Nonetheless, this analysis of the *Chandra* spectrum of H1821+643 provides the first direct evidence (a) that the column density-weighted mean value of  $[f(\text{O VI})]^{-1}$ , is substantially higher than the conservative value of 5.0 that TSJ and Savage et al. (2002) used to derive lower limits on  $\Omega_b(\text{O VI})$ , and (b) that as a result, the baryon fraction associated with O VI absorbers substantially exceeds that of any other known low redshift baryon component, representing an appreciable fraction of the baryons predicted by BBN. The combined column density of the candidate “new” O VII and O VIII lines is comparable to that of the three lines at O VI redshifts, so these systems, if real, would represent a hotter IGM component containing a similar baryon fraction.

The estimate of  $\langle [f(\text{O VI})]^{-1} \rangle$  requires that we treat the  $2\sigma$  lines as real detections. More conservatively, we can derive an upper limit on  $\langle [f(\text{O VI})]^{-1} \rangle$ , without taking a stand one way or the other on the reality of the detections. Of course, since our conservative estimate already implies  $\Omega_b(\text{O VI})$  of the same order as  $\Omega_{\text{BBN}}$ , these upper limits are not very restrictive. For the  $1\sigma$  upper limit, we carry out the sum in equation (6) including  $N(\text{O VIII})$  from the z2 system and  $N(\text{O VII})$  from the z4 system, and we add to it the quadrature

sum of the  $1\sigma$  errors on  $N(\text{O VII})$  and  $N(\text{O VIII})$  for all six systems, dividing the total by  $\sum_i N_i(\text{O VI})$ . For the corresponding  $2\sigma$  upper limit, we simply double the error bars on each system. The result is  $\langle [f(\text{O VI})]^{-1} \rangle < 60$  at  $1\sigma$  and  $\langle [f(\text{O VI})]^{-1} \rangle < 79$  at  $2\sigma$ . In combination with the TSJ or Savage et al. (2002) numbers, even the  $1\sigma$  upper limit is consistent with  $\Omega_b(\text{O VI}) \approx \Omega_{\text{BBN}}$ . If we had obtained null results for all of the O VI systems, then the upper limit on  $\Omega_b(\text{O VI})$  would have come out well below  $\Omega_{\text{BBN}}$ .

O VII lines with observed-frame  $W \gtrsim 26\text{m}\text{\AA}$ , or O VIII lines with  $W \gtrsim 20\text{m}\text{\AA}$ , would have appeared in our data unambiguously, with significance  $\gtrsim 4\sigma$ . We can clearly rule out the existence of such systems along this line of sight. If we exclude the  $22.2 - 23.6\text{\AA}$  region, then the observable path length for the O VII systems is  $\Delta z = 0.2322$  and for O VIII systems  $\Delta z = 0.2232$ . We therefore estimate that the number density of such systems is  $dN/dz < (\Delta z)^{-1} \sim 4$  in each case. For Poisson statistics, the probability of finding no systems where three are expected is  $e^{-3} \approx 0.05$ , so the 95% confidence limit on the density of strong O VII and O VIII lines is  $dN/dz \lesssim 12$ .

In fact, even the existence of the systems that we have detected at the  $2 - 3\sigma$  level is rather surprising relative to theoretical expectations. For IGM metallicity  $[\text{O}/\text{H}] = -1$ , hydrodynamic simulations predict one O VII system per unit redshift above column density  $N \sim 10^{15}\text{cm}^{-2}$ , with a similar result for O VIII, and a rapid decline in the line density for higher column density thresholds. We base this statement on Figure 7 of Chen et al. (2002), but the comparisons in that paper suggest that the Hellsten, Gnedin, & Miralda-Escudé (1998) or Fang, Bryan, & Canizares (2002a) simulations would yield similar results for the same metallicity assumption, at least within a factor  $\sim 2$ . Adding scatter to the IGM metallicities increases the probability of finding strong O VII or O VIII systems, since there are more low (total) column density systems to scatter to high (oxygen) column densities than *vice versa*. With the metallicity scatter predicted by Cen & Ostriker (1999b), the line density predicted by Chen et al. (2002) falls to  $dN/dz \sim 1$  at thresholds of  $N(\text{O VII}) \sim 2 \times 10^{15}\text{cm}^{-2}$  and  $N(\text{O VIII}) \sim 3 \times 10^{15}\text{cm}^{-2}$ . It remains surprising to find 2 – 4 systems (two if we count only those at O VI redshifts, four if we count the candidate “new” systems) with column density in excess of  $4 \times 10^{15}\text{cm}^{-2}$  in a path length of  $\Delta z \sim 0.23$ . The incidence of O VI absorption towards H1821+643 appears to be higher than average (Savage et al. 2002), and the same could be true for O VII and O VIII absorption. Nonetheless, accounting for the systems reported here within the framework of the  $\Lambda\text{CDM}$  cosmological model (or at least the Chen et al. [2002] simulation of it) requires that some regions of the shock-heated IGM be enriched to metallicities several times higher than  $[\text{O}/\text{H}] = -1$ , and it probably requires that the frequency of such enriched regions be higher than the Cen & Ostriker (1999b) model predicts. Confirmation of the observed systems at higher S/N, and correspondingly improved estimates of the O VII and O VIII column densities, would allow firmer assessment



of the theoretical predictions for X-ray forest absorption.

## 5. Conclusions and Outlook

In combination with the *HST* and *FUSE* observations of O VI absorption, this *Chandra* spectrum of H1821+643 provides the most direct evidence to date for the pervasive, moderate density, shock-heated IGM predicted by leading cosmological models. The spectrum shows absorption signals with  $\gtrsim 2\sigma$  significance at the expected wavelengths of O VII and O VIII absorption for one of the O VI systems, at the expected wavelength of O VII absorption for another, and at the expected wavelength of Ne IX absorption for a third. There are two absorption features of comparable strength within  $1000 \text{ km s}^{-1}$  of predicted O VII and O VIII absorption wavelengths, which could represent additional absorbing gas in the large scale environment of the O VI systems. Some of the other  $\sim 2\sigma$  features in the spectrum could correspond to X-ray forest systems without associated O VI absorption, but these features are present in roughly the number expected for Gaussian noise, so without an *a priori* reason to search for absorption at their observed wavelengths, we have no convincing evidence that they represent physical systems. There is a clear detection of Galactic O I absorption, and a strong, broad feature at  $25.35\text{\AA}$  for which we have no obvious identification.

The best estimates of the ratios  $N(\text{O VII})/N(\text{O VI})$  and  $N(\text{O VIII})/N(\text{O VI})$  for the two detected O VI systems imply that they are largely photoionized and that gas densities are significantly below those expected in virialized structures like groups or clusters. This inference relies on the assumption that the O VI, O VII, and O VIII absorption arise in the same gas, not in different components of a multi-phase system. Independent of the single-phase assumption, the measured ratios imply that the column density-weighted mean value of  $[f(\text{O VI})]^{-1}$  is substantially higher than the value of 5.0 that TSJ used to derive their lower limits on  $\Omega_b(\text{O VI})$ , the baryon density associated with O VI absorbers. TSJ and Savage et al. (2002) find  $\Omega_b(\text{O VI}) \sim 0.002 - 0.004 h_{70}^{-1}$  for  $[\text{O}/\text{H}] = -1$  and  $[f(\text{O VI})]^{-1} = 5$ , and our results imply that  $\langle [f(\text{O VI})]^{-1} \rangle = 32 \pm 9$  at  $1\sigma$ . At face value, therefore, our measurements suggest that the baryon fraction associated with O VI absorbers is substantially larger than that in stars, cold gas, or hot gas detected in X-ray emission, and that the O VI absorbers trace a significant reservoir of the “missing” low redshift baryons. The candidate O VII and O VIII systems that are not at the O VI redshifts contain a similar total amount of highly ionized oxygen. In combination with the results of hydrodynamic simulations (Hellsten, Gnedin, & Miralda-Escudé 1998; Fang et al. 2002b; Chen et al. 2002), the existence of even one or two X-ray forest lines at the column densities of our detected systems suggests that some regions of the shock-heated IGM have been enriched to well above  $[\text{O}/\text{H}] = -1$ , and the oxygen and

hydrogen column densities measured for the z2 O VI absorber suggest  $[O/H] \gtrsim -0.3$  in this system.

Unfortunately, our results also show that definitive measurements of X-ray forest absorption are extraordinarily difficult, even with the great technological advance that *Chandra*, LETG, and ACIS-S represent over previous instruments. The absorption signals for the detected O VI systems differ from zero at only the  $2 - 3\sigma$  level, and since we detect some but not all of the known O VI systems, we cannot rule out the possibility that the apparent association between these features and predicted absorption redshifts is simply a coincidence. The features at other wavelengths are not strong enough to represent clear detections of new systems. The constraints on the physical properties and associated baryon fraction of the O VI absorbers are very interesting at the  $1\sigma$  level, but with  $2\sigma$  error bars we obtain only loose constraints that are not particularly surprising, though they are still more than was previously known. *XMM-Newton* has larger effective area than *Chandra* at soft X-ray wavelengths. However, the effective area near  $25\text{\AA}$  is non-uniform, with many instrumental features at observationally interesting wavelengths. Furthermore, published spectra obtained with RGS at these wavelengths seem to achieve lower resolution than *Chandra*/LETG, reducing the sensitivity to narrow lines. It is not clear, therefore, whether *XMM-Newton* will prove as powerful as *Chandra* in X-ray forest searches.

Studies of X-ray forest absorption are among the major scientific drivers for *Constellation-X*,<sup>6</sup> and for the still more powerful *XEUS* mission.<sup>7</sup> *Chandra* and *XMM-Newton* can at best give us a glimpse of what these future missions may achieve. However, the tantalizing but still ambiguous hints of X-ray forest absorption in the H1821+643 spectrum would be frustrating to live with for half a decade or more. In our view, the best step forward in the study of the X-ray forest would be further *Chandra* observations of H1821+643, which remains the best target for such an investigation because of its X-ray brightness and well studied O VI absorption, and because the *Chandra* spectrum presented here provides 500 ksec of existing data and clear objectives for a future observation. For example, an additional 1 Msec observation would reduce the noise in the co-added spectrum by  $3^{1/2}$ , so any true physical features that have  $2\sigma$  significance in the current spectrum would rise to  $3.5\sigma$  significance, making their reality entirely unambiguous, regardless of whether they lie at the redshift of a known O VI system. Conversely, since we obtain  $1\sigma$  upper limits  $N(\text{O VII}) \lesssim 1.9 \times 10^{15} \text{cm}^{-2}$  and  $N(\text{O VIII}) \lesssim 3 \times 10^{15} \text{cm}^{-2}$  for systems with no absorption signal in the current spectrum, the  $1\sigma$  upper limits in undetected systems from a co-

---

<sup>6</sup><http://constellation.gsfc.nasa.gov>

<sup>7</sup><http://astro.estec.esa.nl/SA-general/Projects/XEUS>

added 1.5 Msec spectrum would imply  $f(\text{O VII})/f(\text{O VI}) < 11 [N(\text{O VI})/10^{14}\text{cm}^{-2}]^{-1}$  and  $f(\text{O VIII})/f(\text{O VI}) < 18 [N(\text{O VI})/10^{14}\text{cm}^{-2}]^{-1}$ , respectively. These constraints are still not extremely strong for any individual system, but null detections for all of the known O VI systems in such a spectrum would suggest that the total amount of material they contain is not enough to represent the main reservoir of the missing low redshift baryons.

*Chandra* observations can also guide the design of X-ray forest studies with future missions. If the apparent detections in our current spectrum represent real systems, then *Constellation-X* is likely to find an abundance of X-ray absorption lines tracing the enriched, shock-heated IGM. Conversely, if the evidence for these features weakens as the S/N improves, then tall trees in the X-ray forest are rare, and even *Constellation-X* will have to search long and hard to find them.

We thank the entire *Chandra* team for a superb mission. We are grateful to CXC scientists for extensive help in the data reduction and analysis process. We thank Jordi Miralda-Escudé, Fabrizio Nicastro and Todd Tripp for helpful discussions. This work is supported by Chandra X-ray Observatory Grant GO1-2118X from Smithsonian Astrophysical Observatory. DHW acknowledges the hospitality of the Institut d’Astrophysique de Paris and support from the French CNRS during the completion of this work. X.C. is supported at Ohio State by the DOE under grant DE-FG03-92ER40701, and at ITP/UCSB by the NSF under grant PHY99-07949.

## REFERENCES

- Bahcall, J. N. & Peebles, P. J. E., ApJ, 156, L7
- Brinkman, A.C. et al. 1997, Proc. SPIE, 3113, 181
- Burles, S., & Tytler, D. 1997, AJ, 114, 1330
- Burles, S., & Tytler, D. 1998, ApJ, 507, 732
- Cen, R. & Ostriker, J. P. 1999a, ApJ, 514, 1
- Cen, R. & Ostriker, J. P. 1999b, ApJ, 519, L109
- Chen, X., Weinberg, D. H., Katz, N., & Davé, R. 2002, ApJ, submitted, astro-ph/0203319
- Davé, R., Hernquist, L., Katz, N., and Weinberg, D. H., 1999, ApJ, 511, 521
- Davé, R. et al. 2001, ApJ, 552, 473

- Fang, T. and Canizares, C. R., 2000, ApJ, 539, 532
- Fang, T., Bryan, G. L., & Canizares, C. R. 2002a, ApJ, 564, 604
- Fang, T., Davis, D. S., Lee, J. C., Marshall, H. L., Bryan, G. L., & Canizares, C. R. 2002b, ApJ, 565, 86
- Ferland, G. J., 1999. *Hazy, a brief introduction to cloudy 94*, University of Kentucky, Physics department internal report
- Fukugita, M., Hogan, C. J., & Peebles, P. J. E., 1998, ApJ, 503, 518
- Hellsten, U., Gnedin, N. Y., & Miralda-Escudé, J., 1998, ApJ, 509, 56 (HGM)
- Hernquist, L., Katz, N., Weinberg, D. H., & Miralda-Escudé, J., 1996, ApJ, 457, L51
- Lockman, F. J., & Savage, B. D. 1995, ApJS, 97, 1
- Miyaji, T., Ishisaki, Y., Ogasaka, Y., Ueda, Y., Freyberg, M. J., Hasinger, G., & Tanaka, Y., 1998, A&A, 334, L13.
- Navarro, J. F., Frenk C. S., White, S. D. M., 1997, ApJ, 490, 493
- Nicastro, F. et al. 2002, ApJ, in press, astro-ph/0201058
- Oegerle, W. R. et al. 2000, ApJ, 538, L23
- Perna, R. & Loeb, A., 1998, ApJ, 503, L135
- Press, W. H., Teukolsky, S. A., Vetterling, W. T., & Flannery, B. P. 1992, Numerical Recipes in Fortran, (Cambridge: Cambridge University Press)
- Rauch, M., & Haehnelt, M. G. 1995, MNRAS, 275, L76
- Rauch, M., Miralda-Escudé, J., Sargent, W. L. W., Barlow, T., Hernquist, L., Weinberg, D. H., Katz, N., Cen, R., & Ostriker, J. P., 1997, ApJ, 489, 7
- Richter, P., Savage, B. D., Wakker, B. P., Sembach, K. R., & Kalberla, P. 2001, ApJ, 549, 281
- Savage, B. D., Sembach, K. R., Tripp, T. M., & Richter, P., 2002, ApJ, 564, 631
- Sembach, K. R., Howk, C., Savage, B. D., Shull, J. M., & Oegerle, W. R. 2001, ApJ, 561, 573

Shull, J. M., Roberts, D., Giroux, M. L., Penton, S. V., & Fardal, M. A. 1999, *AJ*, 118, 1450

Tripp, T. M. and Savage, B. D., 2000, *ApJ*, 542, 42

Tripp, T. M., Savage, B. D., & Jenkins, E. B., 2000, *ApJ*, 534, L1

Verner, D. A., Verner, E. M., & Ferland, G. J., 1996, *Atomic Data Nucl. Data Tables*, 64, 1

Weinberg, D.H., Miralda-Escudé, J., Hernquist, L., & Katz, N., 1997, *ApJ*, 490, 564

Weymann, R. J. et al. 1998, *ApJ*, 506, 1

Table 1: Observed EWs of X-ray lines at the redshifts of OVI Absorbers<sup>1</sup>

X-ray Lines	z1	z2	z3	z4	z5	z6 <sup>2</sup>
OVII K $\alpha$	< 6.9	<b>13.9</b> $\pm$ 6.2	< 6.3	7.3 $\pm$ 6.3	< 6.8	<b>9.1</b> $\pm$ 4.7
OVIII K $\alpha$	< 4.7	5.2 $\pm$ 4.9	< 4.9	< 4.9	< 4.9	<b>9.9</b> $\pm$ 5.2
NeIX K $\alpha$	< 3.7	< 3.7	< 3.6	<b>8.4</b> $\pm$ 3.6	< 3.6	< 3.4

1. All EWs are in mÅ, and errors are  $1\sigma$ . Upper limits ( $1\sigma$ ) are listed when best fit values of EWs are zero. “Detected” systems, with significance  $\gtrsim 2\sigma$ , are indicated in boldface type. All EWs are *observed frame* and must be divided by  $(1+z)$  to obtain rest-frame values.

2. The redshifts are: z1=0.26659, z2=0.24531, z3=0.22637, z4=0.22497, z5=0.21326, z6=0.12137. Reference: z1–z5: Tripp et al. (HST); z6: Oegerle et al. (FUSE)

Table 2: Observed EWs of “new” systems<sup>1</sup>

Redshifts	OVII K $\alpha$	OVIII K $\alpha$ <sup>2</sup>
z=0.229048	15.1 $\pm$ 5.8	...
z=0.125847	< 5.3	11.1 $\pm$ 5.0

- Both new redshifts are within  $\sim 1000$  km s<sup>-1</sup> of known OVI redshifts.
- The OVIII K $\alpha$  line in the z=0.229048 system falls in the O I edge.

Table 3: Oxygen column densities in the intervening absorption systems<sup>1</sup>

Redshifts	O VI	O VII	O VIII
0.26659	$5.1 \pm 0.8$	$< 1.9$	$< 2.8$
0.24531	$5.2 \pm 0.6$	$3.9 \pm 1.7$	$3.2 \pm 3.0$
0.22637	$2.4 \pm 0.5$	$< 1.8$	$< 3.0$
0.22497	$19.9 \pm 1.2$	$2.1 \pm 1.8$	$< 3.0$
0.21326	$3.55 \pm 0.81$	$< 1.9$	$< 3.0$
0.12137	$10.0 \pm 2.0$	$2.8 \pm 1.5$	$6.7 \pm 3.5$
0.229048	...	$4.3 \pm 1.6$	...
0.125847	...	$< 1.6$	$7.5 \pm 3.3$

1. The known O VI systems are in the upper part of the table and the “new” candidate systems in the lower part. O VI column densities are in units of  $10^{13} \text{ cm}^{-2}$ . They are taken from TSJ and Oegerle et al. (2000) based on the stronger (1032Å) line of the doublet. O VII and O VIII column densities are in units of  $10^{15} \text{ cm}^{-2}$ . They are derived from the equivalent widths in Tables 1 and 2 assuming that the lines are optically thin (eqs. 2 and 3).

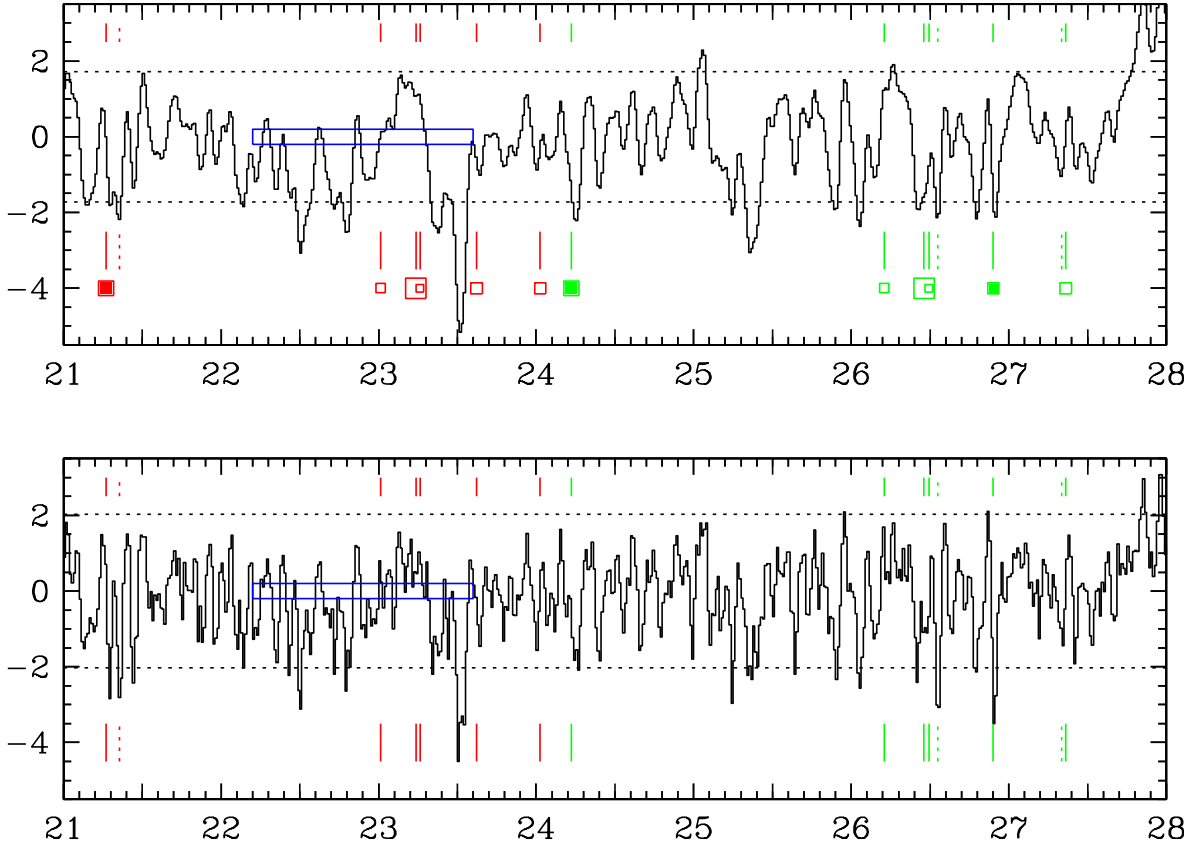


Fig. 1.— Normalized residual spectrum in the 21–28Å region, where O VII or O VIII absorption associated with the known O VI systems towards H1821+643 would lie. The upper panel shows the residual spectrum convolved with the line response function (LRF), a beta function of FWHM=0.05Å (individual channels in the histogram are 0.0125Å). The lower panel shows the residual spectrum convolved instead with a Savitsky-Golay filter, which provides less noise suppression but better preserves the width and depth of spectral features. The blue box in each panel marks a wavelength range (22.2–23.6Å) in which Galactic absorption and instrument response features make accurate continuum modeling difficult; the strong absorption feature at 23.5Å is Galactic O I. In each panel, the residuals are multiplied by a normalization factor such that the range  $-1$  to  $+1$  contains 68% of the data values. Dotted lines mark the symmetric intervals containing 90% of the data values in the upper panel and 95% in the lower panel. Solid line segments mark the expected positions of O VII (green) and O VIII (red) absorption at the known O VI redshifts,  $z_1$  to  $z_6$  from right to left. Squares in the upper panel are proportional in area to the measured O VI equivalent width. Filled squares indicate “detected” systems, for which subsequent analysis shows a line at  $\gtrsim 2\sigma$  significance within the 0.025Å (2-channel) wavelength calibration uncertainty of the expected position. Dotted line segments mark other features of similar strength close to expected O VII or O VIII wavelengths.

05/16/02 17:12



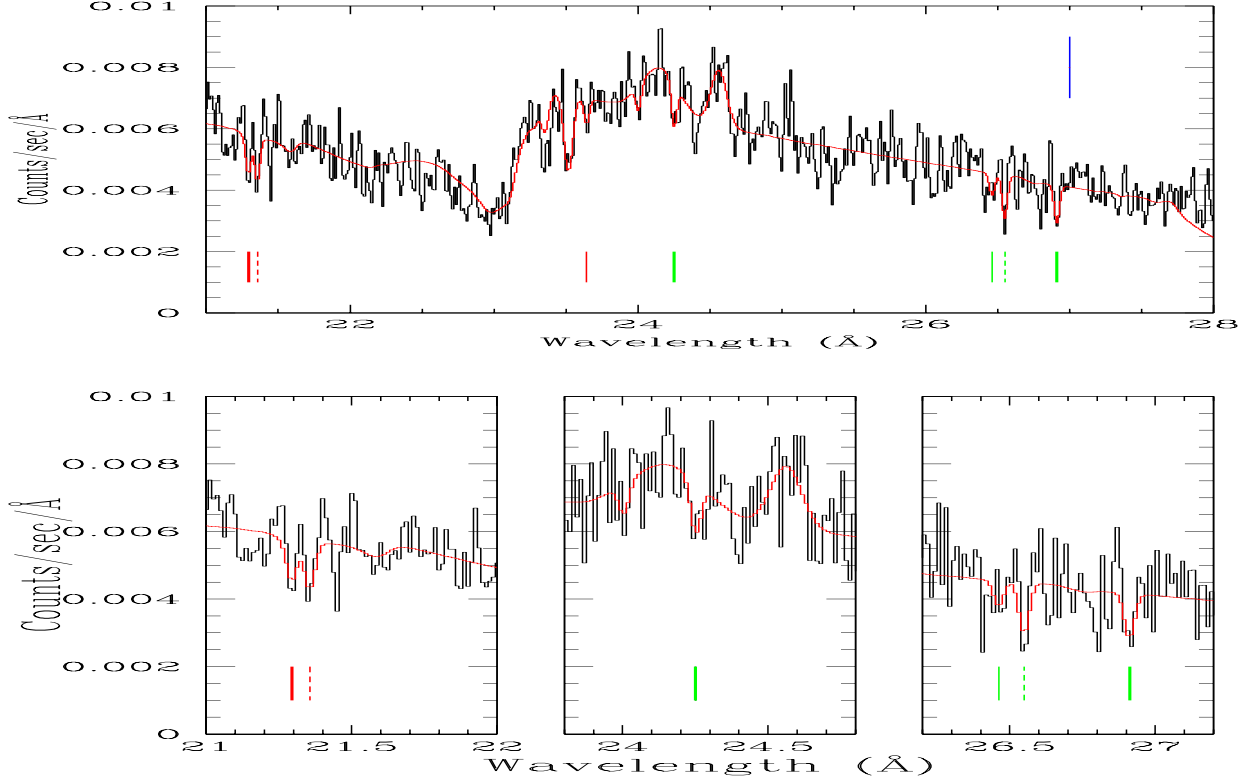


Fig. 2.— Top: The 21 – 28Å region of the observed spectrum, with no extra binning or smoothing. The red line running through the spectrum delineates the continuum + absorption line model fit to the data. The O VII lines are marked in green and O VIII lines in red. The solid tickmarks indicate lines at the known O VI redshifts, with thick lines indicating “detected” systems, whose significance is  $\gtrsim 2\sigma$ . The dashed tickmarks indicate the candidate “new” systems, which are features of comparable strength within  $1000 \text{ km s}^{-1}$  of known O VI redshifts. The broad O I absorption line at  $\sim 23.5\text{Å}$  is from the Galaxy and the O-K edge at  $\sim 23\text{Å}$  is from the instrument as well as the Galaxy. The blue bar in the upper right corner of the figure represents a typical error-bar. Bottom: Zoom on O VIII at  $z6$  (left), O VII at  $z6$  (middle) and O VII at  $z2$  (right) regions showing the detected absorption lines more clearly.

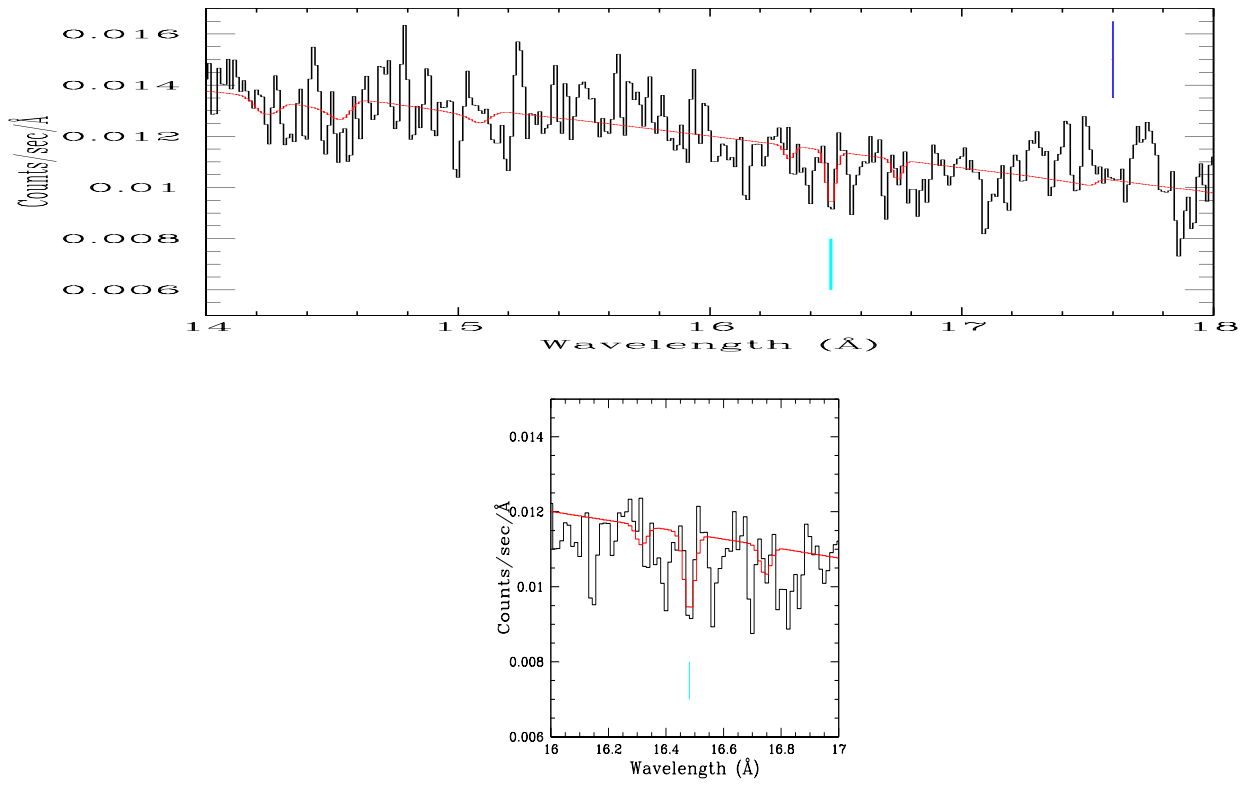


Fig. 3.— Same as Figure 2, but in the NeIX region. The cyan tickmark indicates the “detected” z4 system. Bottom: zoom on the z4 system.

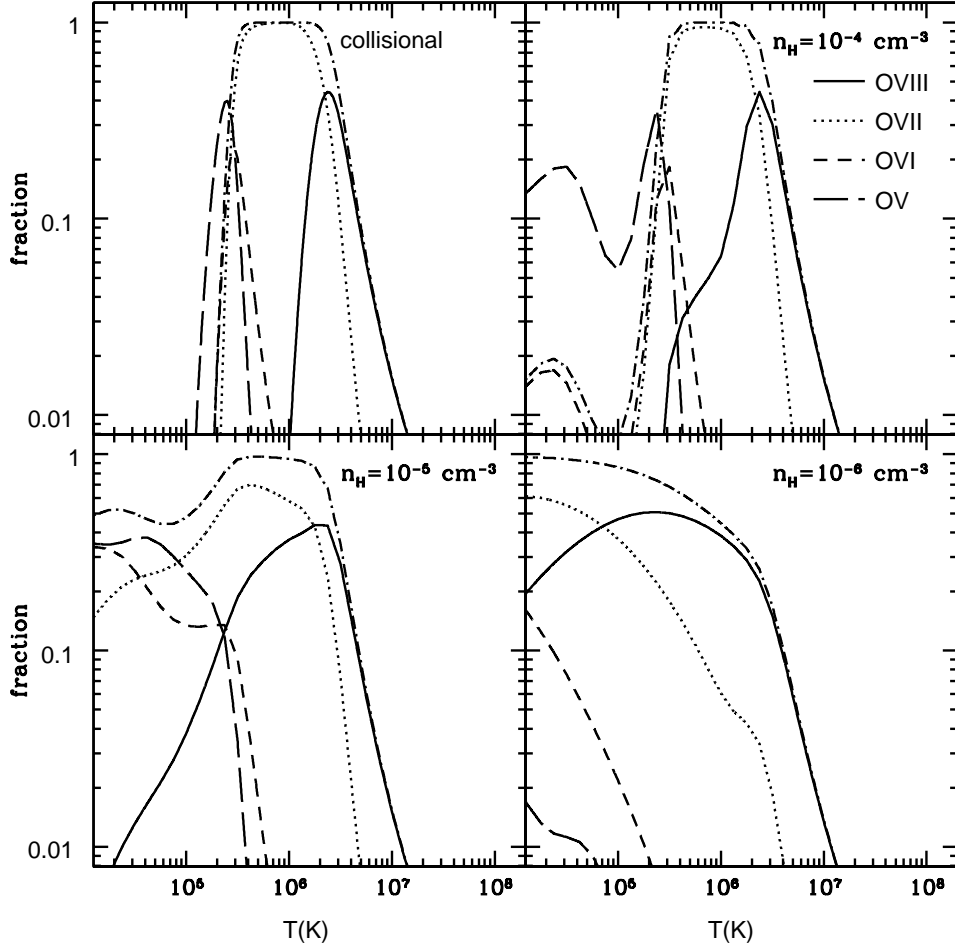


Fig. 4.— Ionization fractions of O V, O VI, O VII, and O VIII as a function of gas temperature. The upper left panel shows results for pure collisional ionization. The other three panels include photoionization by the UV and X-ray background, for gas of density  $n_H = 10^{-6}\text{cm}^{-3}$ ,  $10^{-5}\text{cm}^{-3}$ , and  $10^{-4}\text{cm}^{-3}$ , as marked. The corresponding overdensities are  $\delta_b = 6/(1+z)^3$ ,  $60/(1+z)^3$ , and  $600/(1+z)^3$  for  $\Omega_b h_{70}^2 = 0.04$ . The dot-dashed line in each panel shows  $f(\text{O VI}) + f(\text{O VII}) + f(\text{O VIII})$ , which is close to unity for temperatures  $3 \times 10^5 \text{ K} < T < 2 \times 10^6 \text{ K}$ , and remains high to lower temperatures when  $n_H \leq 10^{-5}\text{cm}^{-3}$ . For details of the calculations, see Chen et al. (2002).

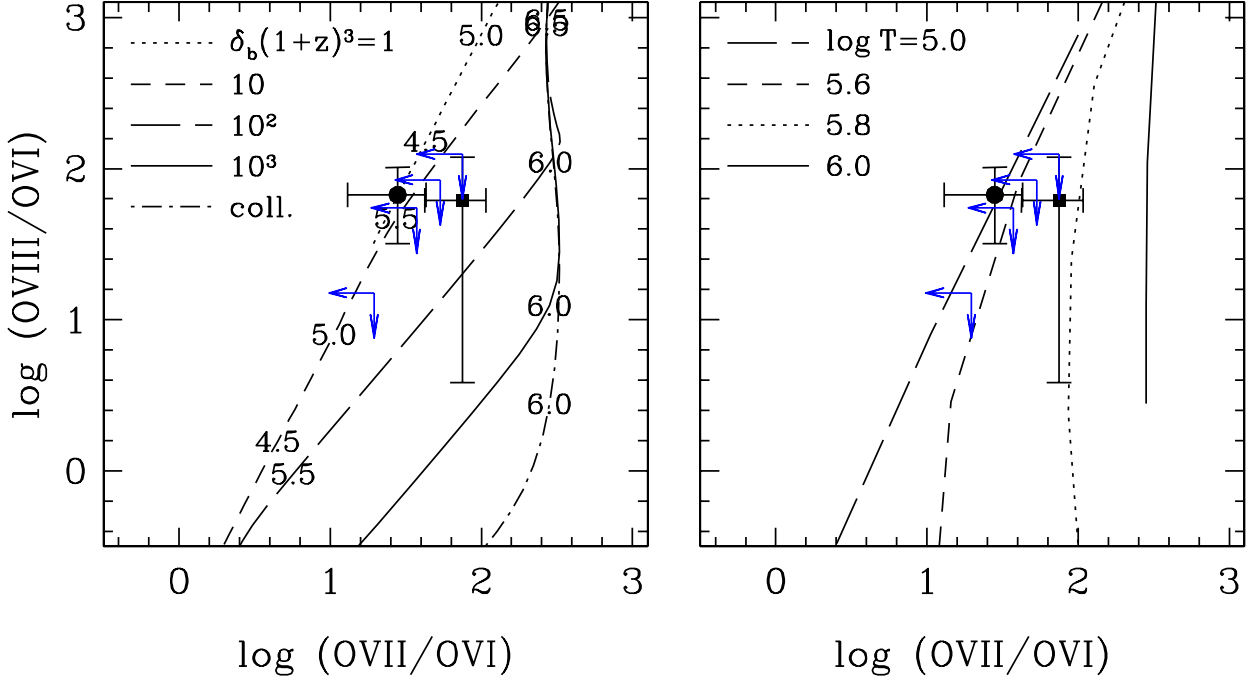


Fig. 5.— Constraints on the physical state of the known O VI absorbers. Left: Curves show the tracks in the  $f(\text{O VIII})/f(\text{O VI})$  vs.  $f(\text{O VII})/f(\text{O VI})$  plane, based on the calculations illustrated in Fig. 4. Dotted, short-dashed, long-dashed, and solid lines are for gas overdensities  $\delta_b(1+z)^3 = 1, 10, 10^2$ , and  $10^3$ , respectively, while the dot-dashed line represents pure collisional ionization. Numbers along these curves indicate  $\log T$  in degrees Kelvin. Points with  $1\sigma$  error bars show the detected systems at  $z_2$  (square) and  $z_6$  (circle); at these redshifts  $(1+z)^{-3} = 0.52$  and  $0.71$ , respectively. Blue arrows indicate  $1\sigma$  upper limits for the remaining four systems, at  $z_4, z_1, z_5$ , and  $z_3$  (bottom to top). Right: Same, but with tracks of constant temperature.

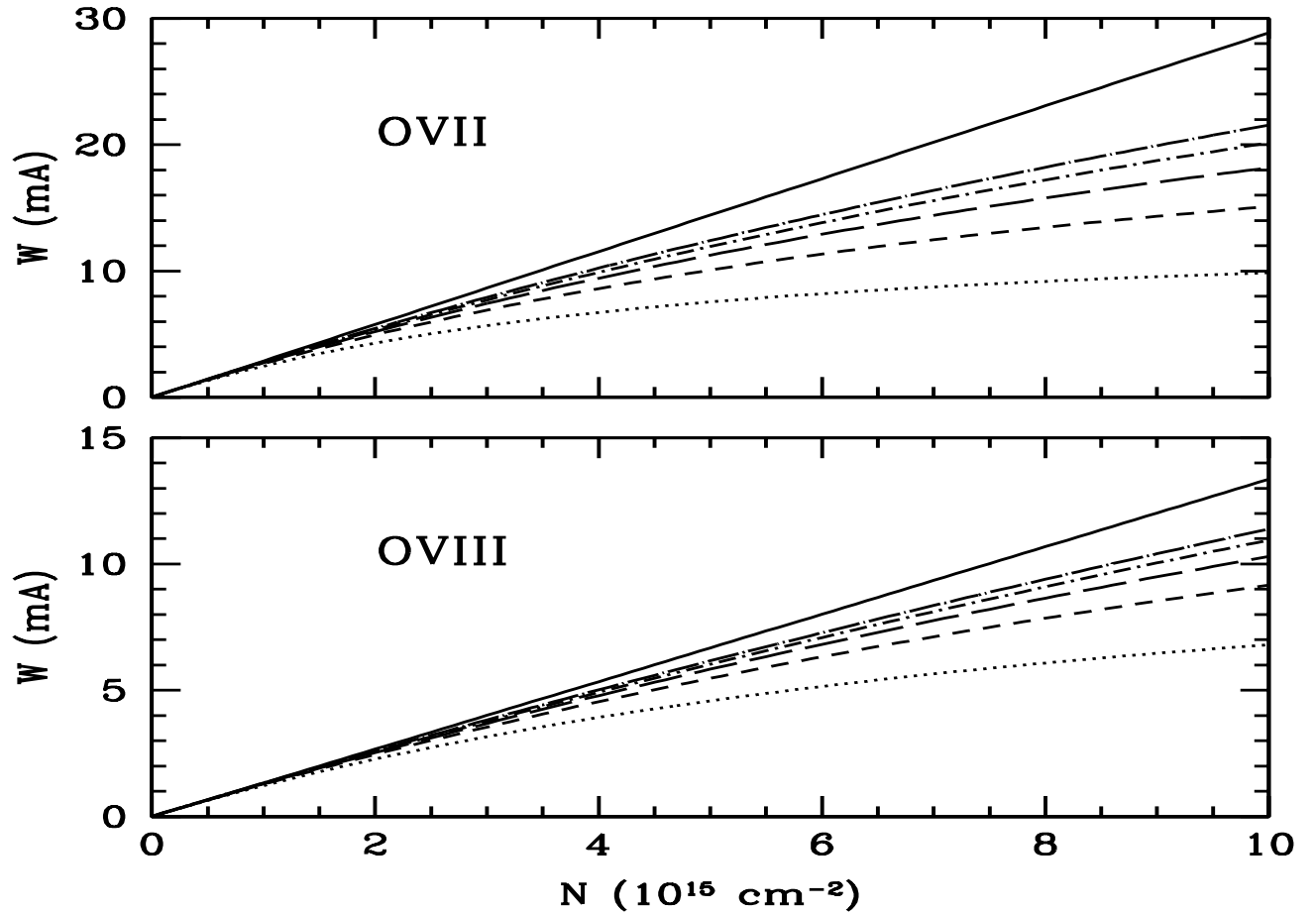


Fig. 6.— Curves of growth for O VII (top) and O VIII (bottom). Absorption line equivalent width is plotted as a function of column density for velocity width parameters  $b = 50, 100, 150, 200, 250$  km s<sup>-1</sup>, from bottom to top. The top curve in both panels is for the optically thin limit.